In-situ Surface Enhanced Raman Spectroscopy Investigations on Surface Transformations of Oxide Derived Copper Electrodes During CO_2RR

Saeede Tafazoli[1,2], Muhammed Yusufoğlu[1,2], Timuçin Balkan[2,3,*], Sarp Kaya[2,3,*]

[1] Materials Science and Engineering, Koç University, 34450 Istanbul, Türkiye

[2] Koç University Tüpraş Energy Center (KUTEM), 34450 Istanbul, Türkiye

[3] Department of Chemistry, Koç University, 34450 Istanbul, Türkiye

*Corresponding authors: sarpkaya@ku.edu.tr (Sarp Kaya), tbalkan@ku.edu.tr (Timuçin Balkan)

Abstract

We investigated the catalytic activity and C2 selectivity in electrochemical carbon dioxide reduction reaction (CO_2RR) on two distinguished electrodeposited Cu oxides with distinct morphologies and structures. The electrode with a compact structure exhibited two times higher faradaic efficiencies of C2 products (40%). Through utilizing electrochemical surface-enhanced Raman spectroscopy (SERS), it was realized that the formation of a metastable phase (malachite) on electrode surfaces by consumption of HCO_3^- could cause a shift in local pH. The analysis of SERS indicated a strong correlation between the presence of the malachite phase and strongly-adsorbed CO on electrode surfaces, preventing dimerization and further reduction. This malachite phase terminating the surface can hinder the charge exchange and interfere with further reductions in C2 products.

Keywords

CO_2 reduction; copper oxide; SERS; malachite; C2 products.

1. Introduction

The ever-growing demand for energy and rising global temperature, driven by released CO_2 in the atmosphere, is one of the world's foremost challenges that must be addressed immediately. CO_2 capturing and converting to fuels have been considered an inevitable part of all proposed solutions. CO_2RR to fuels such as ethylene (C_2H_4), ethanol (C_2H_5OH), and propanol (C_3H_7OH), coupled with renewable electricity resources such as solar cells, can provide an opportunity to abate CO_2 emissions and close the carbon cycle. Due to their potential to generate hydrocarbons electrochemical CO_2RR on copper (Cu) and Cu oxide electrocatalysts has recently attracted tremendous attention [1–3]. Substantial effort has been devoted to understanding the catalytic performance and deciphering the mechanism behind the hydrocarbon generation on these electrocatalysts. C2+ hydrocarbons such as C_2H_4, C_2H_5OH, and C_3H_7OH have attracted more attention than C1 products such as carbon

monoxide (CO), methane (CH_4), methanol (CH_3OH) and formic acid (HCOOH) arising from the CO_2 electroreduction process, due to being more energy-efficient and having lower toxicity [4,5]. It has been claimed that oxide-derived Cu can provide active sites for the C2+ products, which has been driven by the reduction of Cu oxide [6–10].

The morphology and oxidation state of Cu oxides in the first place can play a prominent role in product selectivity. Cu_2O structures in different morphologies, such as nanocubes [11] and hollow nanoparticles [12] that are more durable have been used as electrode materials to achieve the desired selectivity and efficiency. It has been shown that oxide-derived Cu surfaces with high surface area promote CO_2RR compared to the metallic forms due to higher number of uncoordinated sites, steps, kinks, etc. It is however not clear if those oxide-derived roughened surfaces introduce new sites that are more active and selective toward C2+ products [13]. The reduced crystallite sizes could also improve selectivity due to more diverse CO adsorption sites [14].

Multiple computational and experimental investigations have assigned C2 products to the oxidation state of Cu [15–19]. However, a profound relation between the different surface chemical states of Cu and accompanying surface intermediates of CO_2RR is still missing. In addition to this, there are experimental and computational studies showing the role of the Cu oxide phase during the CO_2RR at different potentials and its impact on catalytic behavior and product selectivity [13,20–23], demonstrating co-existing surface Cu species at different chemical states can be a key parameter for higher selectivity towards C2+ products [24]. Cu^0 and Cu^+ in atomic proximity during CO_2RR have been suggested as the main road to CO dimerization, leading to C_2H_4 [8]. The rate of C2+ product formation has also been associated with the hydrogenation of adsorbed CO rather than dimerization [25]. Several ex-situ and quasi-in-situ investigations indicate that Cu oxides get reduced to their metallic state after CO_2RR [26–28]. According to these investigations, higher activity over oxide-derived Cu under reducing conditions stems from the induced roughness. However, whether the surface and/or subsurface oxygen species of oxide-derived Cu contribute to CO_2RR under reducing conditions remains controversial. They could be indispensable to keeping Cu^+ species stable. In-situ spectroscopies such as surface-enhanced Raman spectroscopy (SERS), X-ray absorption spectroscopy (XAS), ambient pressure X-ray photoelectron spectroscopy (AP-XPS) [29–34] have been employed to probe the chemical state of the Cu surfaces. Surface oxygen species promoting CO_2RR and subsurface Cu oxide and Cu-OH species forming depending on the applied potentials have been shown [18,34–36].

The implementation of in-situ techniques can shed light on the adsorbed species, intermediate (metastable) phases, and reaction mechanisms [29,37–43]. Electrochemical experiments can be coupled to the SERS, offering sensitivity to realize the bond vibrations specifically for the lower frequencies (less than 800 cm^{-1}) to discover the Cu oxidation states. Despite numerous research through in-situ SERS over Cu (oxide) electrocatalysts, a few studies report the appearance of metastable copper carbonate hydroxide phases (CCH), such as malachite ($Cu_2(CO_3)(OH)_2$) and azurite ($Cu_3(CO_3)_2(OH)_2$). The first report of this metastable phase was published in 1997 and introduced it as a poisoning species on top of Cu for CO_2RR [44]. This phase has been investigated through XPS [18,45,46], X-ray diffraction (XRD) [47–50], X-ray absorption spectroscopy (XAS) [51,52], and Raman spectroscopy [49,53,54] techniques. Among the studies on this compound, there is a debate about the effect of these species on CO_2RR products. It has been reported that CCH can enhance the activity of the catalyst towards C2 products by CO formation and further CO-CO dimerization [53]. $Cu_2(CO_3)(OH)_2$ developing slowly (48h) on a metallic Cu has given rise to increased faradaic efficiencies (FEs) of C_2H_4 and ethane (C_2H_6) (at low percentages, 1% to 10%) due to the better adjustment of the binding energy of adsorbed intermediate species [55]. In another study, $Cu_2(CO_3)(OH)_2$ was introduced as an active phase to form CO as a product. The formation of CCH motifs promoted by the residual Cu oxides was attributed to the reason for enhanced CO_2RR FEs [53]. However, some investigations record a drop in FEs. Vélez et al reported a significant FE drop due to the severe charge hindrance in the presence of CCH on the surface as a blocking layer [51]. Moreover, Eilert [52] and coworkers showed no significant CCH-induced enhancement in FEs. Henckel [54] and coworkers claim that Cu^{2+} dissolves and reprecipitates as $Cu_2(CO_3)(OH)_2$ in the presence of CO_3^{2-} and its formation depends on the local pH. Therefore, fundamental examinations of the origin and the true effect of the CCH phase on the CO_2RR intermediates and final products are still missing in the literature.

Herein, we demonstrated an in-situ surface monitoring of the two electrodeposited Cu oxides (electrodeposited at a constant current density of -0.9 $mA.cm^{-2}$ for 111 minutes (low CD) and -5 $mA.cm^{-2}$ for 20 minutes (high CD)) before, during, and after CO_2RR. This process simultaneously provided information about the Cu oxidation state, surface intermediates, the formation of possible surface phases, electrode potential, and local pH changes. As complementary measurements, gas chromatography (GC) and proton nuclear magnetic resonance (H-NMR) investigations were employed to determine the final products of the electrodeposited Cu oxides as a function of cathodic potential. This investigation emphasized

the significant impact of the characteristics of the electrocatalyst (morphology, composition, and crystal structure) on the intermediate species and eventual products. The origin of a considerable difference in C2 FEs between two Cu oxide electrocatalysts and the critical surface blocking behavior of the CCH phase were identified through a combination of product and in-situ SERS analysis.

2. Experimental Sections

2.1. Sample preparation

A three-electrode setup with a Ag/AgCl (saturated KCl) reference electrode (RE) was used in electropolishing Cu foils and Cu oxide electrodeposition steps. The polycrystalline Cu foil (25 µm thick, > 99.99%, MTI) as the working electrode (WE) was electropolished in H_3PO_4 solution (≥85%, ISOLAB) at +1.5 V vs. Ag/AgCl for 3 minutes. Polycrystalline Cu with the same geometrical surface area was used as the counter electrode (CE). Immediately, the electropolished Cu foil was rinsed with DI water for 5 minutes and subsequently used as a WE for the electrodeposition of Cu oxides. During electrodeposition, a spiral Pt wire was used as a CE. Cu oxide solution was prepared through a 0.4 M cupric sulfate ($CuSO_4.5H_2O$) (≥ 99.0%, ISOLAB), and 3 M lactic acid (≥ 88%, ISOLAB). Then pH was adjusted to 10.5 by adding 5 M NaOH (≥ 99.0%, ISOLAB). To stabilize the pH, the solution was rested for one night. Two different constant current density of – 0.9 $mA.cm^{-2}$ for 111 minutes (low CD) and -5 $mA.cm^{-2}$ for 20 minutes (high CD) at 40 °C was applied (SP-200 BioLogic, CP method). The geometric surface area of foils was around 1 cm × 1 cm for each WE. Impurities of precursors of this electrodeposition are tabulated in Table S1.

2.2. Sample characterization

To characterize the morphology of the surface and measure the thickness of electrodes, scanning electron microscopy (SEM, Zeiss Ultra Plus with an accelerating potential of 20 kV) was employed. X-ray diffraction (XRD) patterns of the electrodes were collected using Bruker D8 Advance X-Ray Diffractometer. The measurements were done at a normal incidence angle and Cu Kα radiation (λ = 0.15406 nm) was the X-ray source. X-ray photoelectron spectroscopy (XPS) analysis was performed by utilizing a Thermo K-alpha laboratory XPS system equipped with a monochromatized Al Kα X-ray source (hν = 1486.7 eV). To avoid charging, an automated flood gun was used. Pass energy was set at 50 eV for the presented regions.

2.3. Electrochemical measurements

A customized H-type electrochemical cell was used for CO_2RR studies. Cathodic and anodic compartments were separated by an ion-exchange membrane, Nafion 212 (Fuel Cell Store). The electrodeposited Cu oxide (1.0 cm × 1.0 cm), a Ag/AgCl, and a spiral Pt wire were utilized as WE, RE, and CE, respectively. 70 ml of 0.5 M $KHCO_3$ (99.51%, Sigma Aldrich, Impurities are tabulated in Table S2.) was used as an electrolyte and purged for 20 minutes prior to each measurement. 20 $ml.cm^{-2}$ flow of CO_2 gas (99.99%, Airliquid) was fed into both the cathodic and anodic compartments through a manual flowmeter. Potentials applied through chronoamperometry method by SP-200 BioLogic potentiostat.

To provide the same condition for both electrodes, Cu oxide electrodes were pre-reduced at -0.45 V to reach a stable current. Gas products were detected and quantified using a gas chromatograph (GC, Agilent7820A) equipped with a thermal conductivity detector (TCD) and flame ionization detector (FID). Through Nuclear Magnetic Resonance (NMR) spectrometer (Bruker AVANCE NEO 500MHz) liquid products were analyzed. The liquid products were dissolved inside the cathodic electrolyte mixed with deuterated water (D_2O) in the presence of dimethylsulfoxide (DMSO) as an internal standard. The details of the quantification of the gaseous and liquid products are provided below. Cu content in the electrolyte was determined using an inductively coupled plasma-mass spectrometer (ICP-OES) analyzer (Agilent 7700x).

All the potentials were converted to the reversible hydrogen electrode (RHE) reference through the following Nernst equation:

$$E_{RHE} = E_{Ag/AgCl} + (0.059 \times pH) + E^{\circ}_{Ag/AgCl}$$

$E^{\circ}_{Ag/AgCl}$ is the thermodynamic standard reduction potential (0.197 V). The uncompensated solution resistance ($R_u \approx 6\ \Omega$) was measured by single-point impedance at 100 kHz. This measurement was performed before each potential application and automatically corrected 85% of the iR_u drop (i: current). The contribution of the remaining 15% to the electrode potential was calculated 0.05 and 0.04 V for the low CD and high CD electrodes, respectively (see the SI for details).

2.4. Electrochemical surface area (ECSA) measurement

The Electrochemical surface area was measured in a non-faradaic region near OCP from 0.5 to 0.6 V vs. RHE. The cyclic voltammetry at different scan rates of 20, 40, 60, 85, and 100 mV/s was applied with the same CO_2RR condition for the electrode. Through this experiment, we were able to calculate the double-layer capacitance (C_{dl}). At the same measured voltage,

capacitive currents (anodic and cathodic) to the different voltage scan rates were plotted and the slope of the plots was calculated as the C_{dl}. By dividing the derived C_{dl} by the ideal Cu_2O capacitance (40 $\mu F.cm^{-2}$) ECSA amount will be calculated [56].

$$ECSA = \frac{C_{dl}}{40\ (\mu F.cm^{-2})}$$

3. Results and Discussion

The chemical states of Cu can have a substantial effect on boosting the C2 product selectivity in the CO_2RR [57–59]. XRD measurements were applied to study Cu oxide phases before and after CO_2RR. XRD patterns presented in Figure 1a indicate that both as-prepared electrodes represent Cu_2O (cuprous oxide) coexisting with the CuO (owing to (200) at 42.5° and ($\bar{1}13$) at 61.6° facets) and metallic Cu (owing to (111) at 43.5°, (200) at 50.6°, and (220) at 74.5° facets) originated from Cu foil used as a substrate. One characteristic peak at 29.9° for the electrodes before CO_2RR can be assigned to the (110) facet of Cu_2O. After CO_2RR (90 minutes at -0.8 V vs. RHE), a low-intensity peak of Cu_2O ((111) at about 37°) was detected in the high CD electrode whereas low CD Cu oxide has been fully reduced to metallic Cu exhibiting (111) at 43.5°, (200) at 50.6°, and (220) at 74.5° facets.

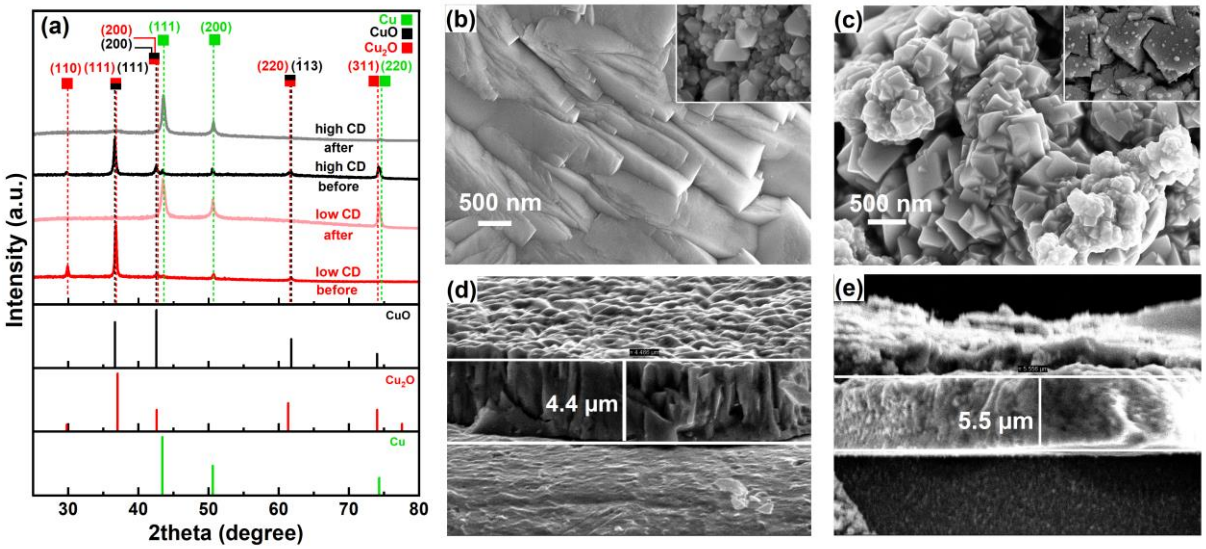


Figure 1. (a) XRD pattern of the electrodes before and after CO_2RR at -0.8 V vs. RHE for 90 min. Top view SEM images of the (b) as-prepared low CD Cu oxide (prolonged cubes), (c) as-prepared high CD electrode, and (d) and (e) their thickness determined by cross-sectional imaging, respectively. Insets in (b) and (c) are top views of the same electrodes after CO_2RR with the same scale.

Through scanning electron microscopy (SEM), it is possible to monitor morphological differences between as-prepared and tested electrodes. Figure 1b shows a compact one-

directional growth for the low CD electrode. This morphology can be explained by the sparse nucleation accompanied by the lateral growth due to the lower current density at the nucleation step [60]. Morphology of the high CD electrode, on the other hand, indicates a porous structure of cubic Cu oxides (multiple nuclei). The growth behavior of two Cu oxides could be explained by the fact that electrodeposition of the low CD electrode, due to the applied lower current density, started with a fewer number of nuclei [61,62] than the one with the high CD and due to the more extended deposition period (to keep the charge at the same amount), these nuclei had enough time to grow through preferable facets. Although the time of deposition for the low CD electrodes is about five times longer than the high CD, the thicknesses of the Cu oxide layers are similar to each other since the same amount of charge was withdrawn for both (Figure 1d and e). After the CO_2RR, morphological changes on both electrode surfaces were observed. Nanoparticles (NPs) on the surface of the cubes present on the high CD electrode could be resulting from Cu NPs oxidized once exposed to the ambient air [54,63].

To further analyze the chemical states of the electrode surfaces, XPS measurements were employed. According to the Cu 2p XPS spectra presented in Figure 2a, the peak at 932.4 eV and small satellite feature centered around 945 eV confirm that Cu_2O is the primary component of as-prepared electrodes. Cu 2p XPS spectra also reveal high binding energy shoulder peaks at 934.2 eV that could be attributed to CuO on both as-prepared surfaces, with higher intensity for the surface of the low CD electrode. Furthermore, intense satellite peaks between 940-944 eV for the as-prepared low CD electrode confirm the existence of CuO. Cu 2p XPS spectra are not very sensitive to distinguish metallic Cu from Cu_2O, however, Cu LMM Auger spectra shown in Figure 2b lack the distinct feature at around 918.4 eV kinetic energy which indicates the surface of the as-prepared electrodes does not have metallic Cu. Cu LMM Auger spectra show the main peak at 916.7 eV kinetic energy which is characteristic of Cu_2O. We note here that, although samples were kept in N_2 until the XPS measurement, they can be in contact with the ambient air while placing them inside the XPS setup. Also, Auger spectra of both as-prepared electrodes showed a peak at 917.7 eV related to CuO (weaker in high-CD electrode), in accordance with the XPS spectra. Due to their higher kinetic energy, Auger electrons have a higher penetration depth, one can thus conclude that the surfaces of both electrodes contain CuO with a varying thickness (2-3 nm) but their bulk is Cu_2O. Metallic Cu features were observed in Cu LMM Auger spectra after CO_2RR but full metallization was not observed. The main Cu $2p_{3/2}$ peak at 932.2 eV gets intensified for

both low and high CD electrodes after CO_2RR, high binding energy shoulder of the latter remains more prominent.

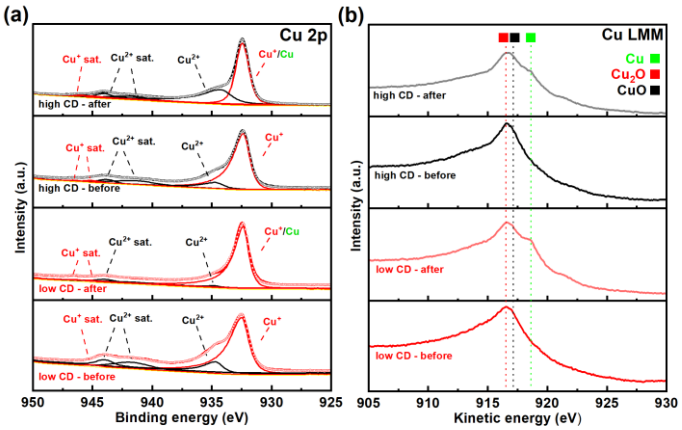


Figure 2. (a) Cu 2p XPS and (b) Cu LMM Auger spectra of the as-deposited Cu oxide electrodes and spectral changes obtained after CO_2RR (90 min at -0.8 V vs. RHE).

Figure 3 shows the FE distribution of all detected CO_2RR products over both electrodes at different potentials. Hydrogen evolution reaction (HER) starts at -0.5 V and hydrogen formation gradually increases with increasing cathodic potentials. This can be an indication of suppressing CO_2RR by HER for both electrodes. However, a higher rate of HER was obtained on the high CD electrode. In agreement with the general trend reported, our results support that low-coordinated Cu sites formed by further reduction of the primary Cu oxide at high overpotentials are in favor of HER over CO_2RR [64]. This also agrees well with the high local pH estimated over both electrodes, which will be explained in the following section. Increased HER activity at high cathodic potentials can be explained by the roughness of Cu electrodes, as explained above. More importantly, concentrated electrolytes (0.5 M $KHCO_3$) involving anions with high buffering capacity provide protons, which impact positively the rate of the HER [65].

On the high CD electrode, the reduction of CO_2 in the potential range studied starts with the formation of carbon monoxide (CO, FE = 14%), formate ($HCOO^-$, FE = 20%), and acetate (CH_3COO^-, FE = 11.5%) at -0.5 V. Low CD electrode shows similar behavior for CO and $HCOO^-$ but with lower FEs. Increasing cathodic potential leads to a drop in FEs of CO, $HCOO^-$, and CH_3COO^- (for the high CD electrode) whereas it boosts the formation of C2 products, ethylene (C_2H_4), ethane (C_2H_6), propanol (C_3H_7OH), and lastly ethanol (C_2H_5OH) start to appear on both electrodes. This C2 product formation is more prominent on the low CD electrode. Eventually, at -0.9 V, C2 products reach their maximum. This simultaneous

rise and drop in respective FEs of CO and C2 products demonstrate potential dependent change in the product selectivity [66–69]. The recorded FEs for the C2 products on the low CD electrode are twice higher (ca. 40%) than those on the high CD electrode under the same conditions. Low FE (about 40% and less) has been reported over Cu oxides with similar structural features and preparation methods to our electrodes [6,8,35]. Higher FEs for the C2 products have been achieved on unique structures such as dendritic or branched Cu oxides [7,9,57,70] which is usually related to the higher surface area.

At higher cathodic potentials (up to -0.9 V) the FE of C_2H_4 was enhanced. Under these cathodic conditions and high electrolyte concentration (0.5 M $KHCO_3$), high proton concentration plays an important role in the formation of C_2H_4. CO protonation could thus be the critical step in the formation of C_2H_4 at higher cathodic potentials. Methane (CH_4) with low FE (1%) was only detected at the highest overpotential at -1.2 V through a sequential chronoamperometry (Figure S1a). To reveal the origin of these activity differences toward C2 products, in-situ SERS measurements were carried out for both electrodes. The CO_2RR activity of the electropolished Cu foil (the substrate of the electrodeposited electrodes) was also investigated as the reference sample. This measurement was carried out with the sequential method and the results are depicted in Figure S1b. GC results show that CH_4 and H_2 are the only gaseous products detected over this electrode, confirming the reported activities are intrinsic to the oxide-derived electrodes and indicating a low CO_2RR activity of the bare Cu foil. This result was expected because the surface of the Cu foil was electropolished before CO_2RR and before the electrodeposition steps. This process will provide a smooth surface and eliminate the effects of induced roughnesses in C2+ product selectivities. The higher roughness would cause larger surface areas which promote the higher current density required for CO dimerization and discourage HER [26,71,72], while herein, we deliberately prevent the high roughness by electropolishing.

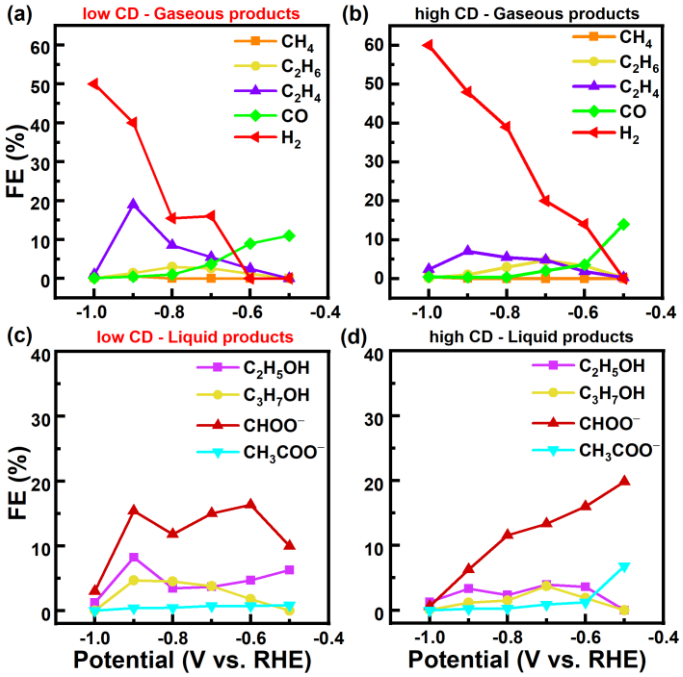


Figure 3. FEs of all detected gaseous products of (a) low CD and (b) high CD and liquid products of (c) low CD and (d) high CD as a function of cathodic potential.

First, the two as-prepared electrodes were examined through SERS in dry and wet forms using a custom-designed electrochemical cell (Figure S2). The features in Raman spectra of Cu oxides are associated with the motions of oxygen atoms in the unit cell. As can be seen in Figure 4a, the low CD electrode represents the identical peaks at ca. 145 (T_{1u}), 220 (E_u), 412 (multiphoton), 520 (T_{2g}), and 645 cm^{-1} (T_{1u}) for Cu_2O in dry and wet conditions. E_u and T_{1u} modes which represent the rotation of Cu tetrahedra around their centers are very sensitive to structural changes. A_u represents oscillations of the central Cu atoms and T_{2g} oxygen sublattice motions. The presence of all these peaks confirms both XRD and Cu LMM Auger spectra, Cu_2O is the primary bulk phase of both electrodes, however, the broad peak at around 631 cm^{-1} (B_g) can be assigned to oxygen vibration in CuO, confirming its presence on the surface as previously demonstrated by Cu 2p XPS spectra (Figure 2a). A red shift in 412 and 645 cm^{-1} peaks in the SERS spectrum of dry high CD electrode could be the indication of the presence of the Cu vacancies (V_{Cu}). The origin of this defect could be attributed to the faster kinetics of high CD deposition. Another peak at about 290 cm^{-1} has been detected for both low and high CD electrodes which can be assigned to the oxygen vibration (A_g mode). Based on results obtained from XRD, XPS, and Raman spectroscopy at different probing depths, we conclude that a thin layer (2-3 nm) of CuO is uniformly covering the surface of the low CD electrode while for the high CD electrode, a thinner CuO layer is present on the surface but

there could be Cu_2O exposed. This transformation also leads to an increased amount of HCO_3^- species on the high CD electrode surface (Figure S3).

Interestingly, after placing the high CD electrode into the electrolyte solution, a structural change was observed. Peaks arising at 540 cm^{-1} (A_{1g}) and 318 cm^{-1} (E_g) indicate the conversion of the Cu_2O (dry) to a metastable phase of Cu_4O_3 (paramelaconite). Cu_4O_3 is a mixture of both Cu^+ and Cu^{2+} ($Cu_2^+Cu_2^{2+}O_3$) and A_{1g} mode of Cu_4O_3 represents oxygen motions along one axis while oxygen motion along the two-folded axis is E_g mode [73]. One possible reason that can be attributed to this conversion is the porous structure of the high CD electrode and mildly basic electrolyte. More importantly, Cu_2O is exposed on the surface of the high CD electrode and therefore it goes through this oxidation process. A full understanding of the mechanism of the formation of Cu_4O_3 cannot be elucidated from our current experiment. However, as seen in Figure 4b, this metastable phase gets promptly converted to CuO (with the main peaks at 290, 345, and 631 cm^{-1}) with a small residual Cu_4O_3. Cu^{2+} exhibits higher hydration energy in aqueous solutions with respect to Cu^+ due to the higher charge density [74], therefore; CuO is more stable in the alkaline solution and its formation could be expected.

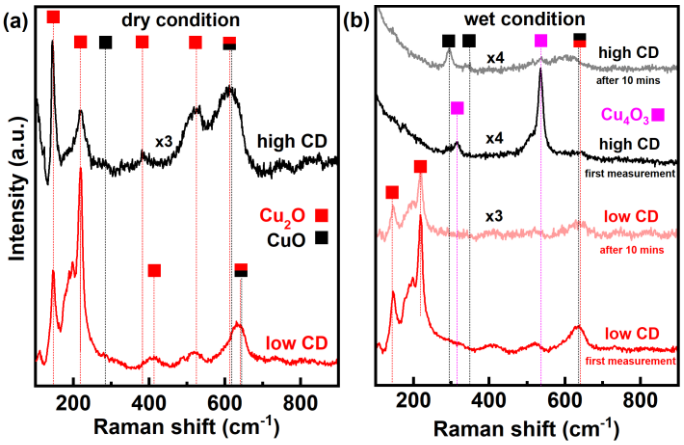


Figure 4. SERS spectra of low and high CD electrodes under (a) dry and (b) wet conditions. SERS spectra in (b) were obtained after immersing electrodes into the 0.5 M $KHCO_3$ electrolyte.

Vibrational features of Cu oxides forming on electrode surfaces, electrolyte, and pH-dependent HCO_3^- / CO_3^{2-} surface/near surface species, and adsorbed surface intermediates of the CO_2RR including adsorbed CO (*CO) can be identified by in-situ SERS under varying cathodic potentials [41,54,75–77]. Figure 5 reports the progression of the SERS features in different frequency regimes. It is worth stating that, in wet measurements under open circuit conditions, the reduced SERS effect on the Cu oxide surface makes peak intensities not

comparable to those obtained from the reduced Cu at cathodic potentials, thus, comparison of the spectra before and after reduction in the same intensity scale is challenging.

At -0.1 V, over the high CD electrode, all CuO and Cu_2O (E and A) disappear immediately, while on the low CD electrode the reduction of Cu_2O (A) takes place at higher cathodic potentials (ca. -0.3 V). This behavior can be explained by the compact and porous structure of the low CD and high CD electrodes, respectively. Concurrently, a CO_3^{2-} peak (B) at 170 cm^{-1} representing the lattice mode vibration appears. The existence and intensity of this peak are in absolute agreement with the other CO_3^{2-} peak at 1070 cm^{-1} in all SERS spectra. On both electrodes, the appearance of the CO_3^{2-} species coincide with the disappearance of the Cu_2O features and they remain on the surface up to -0.9 V. Also, they seem to be more intense on the high CD electrode. In Figure 5b two strong peaks become apparent immediately after applying -0.1 V at 350 (D_1) and 703 cm^{-1} (D_2). These are accompanied by a third peak at ca. 1540 cm^{-1} (D_3) (Figure 6b) and they all originated from adsorbed carboxylate species ($*CO_2^-$). These peaks are assigned to Cu-C vibration, in-plane bending, and asymmetric stretching modes, respectively [43,75]. At -0.5 V and above, $Cu(OH)_2$ peaks at 280 cm^{-1} (E_1) and 480 cm^{-1} (E_2) appear in the spectra of the high CD electrode. We assign the third peak at 550 cm^{-1} (E_3) to $Cu(OH)_2$, however, similar surface features have also been attributed to carbon-containing adsorbates [29,43,78]. Another intense peak at 525 cm^{-1} (C) appears at -0.9 V and stays intact up to -1.1 V which interestingly indicates the formation of an intermediate phase of $Cu_2(CO_3)(OH)_2$ (Cu-OH vibration) [79]. The formation of $Cu_2(CO_3)(OH)_2$ precedes the disappearance of CO_3^{2-} on this electrode. On the other side, none of these peaks has been seen over the low CD electrode within the same potential regime [40] except $Cu(OH)_2$ (E_1) peak observed at 285 cm^{-1} at a very high cathodic potential (-1.1 V). Moreover, CO_3^{2-} species persist on the surface up to very high potentials (-1.1 V) and even at OCP condition after reduction. On both electrode surfaces, the broad peaks at 530 and 600 cm^{-1} (A) reappear after going back to the open circuit conditions and remain when the electrodes are dried.

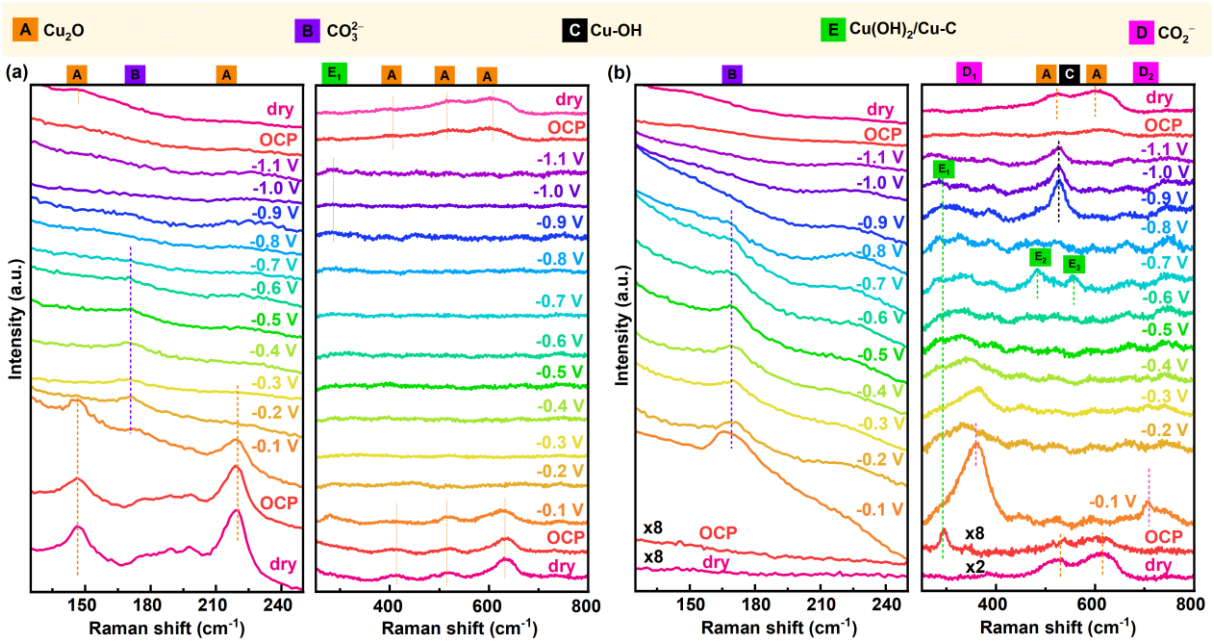


Figure 5. SERS spectra of two electrodeposited Cu oxide electrodes in CO_2-saturated 0.5 M $KHCO_3$ (pH 7.6) electrolyte solution at various cathodic potentials: (a) low CD and (b) high CD electrode. To make a clearer comparison, spectra within 250-800 cm^{-1} were background-subtracted.

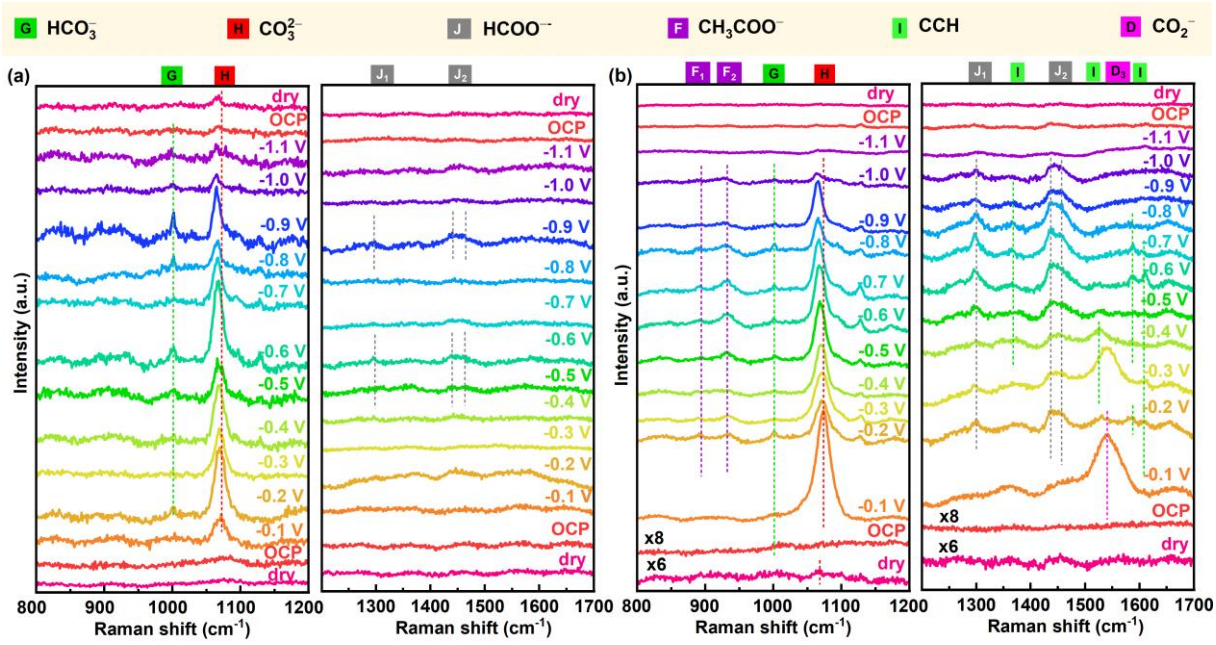


Figure 6. SERS spectra of two electrodeposited Cu oxide electrodes in CO_2-saturated 0.5 M $KHCO_3$ (pH 7.6) electrolyte solution at various cathodic potentials: (a) low CD and (b) high CD electrode. To make a clearer comparison, all spectra within 800-1700 cm^{-1} were background-subtracted.

In Figure 6a and 6b, peaks at 1000 and 1070 cm^{-1} assigned to HCO_3^- (G) and C−O symmetric stretching of CO_3^{2-}(H), respectively, appear at different potentials in SERS spectra for both low and high CD electrodes. HCO_3^- and CO_3^{2-} peaks dominate the spectral region already at -

0.1 V and their intensities change with the potential applied. This intensity modulation might be dependent on the spontaneous change of the SERS effect. Redshift of the CO_3^{2-} peak at higher cathodic potentials can be due to the stark effect under the applied potential field (resulting from a C–O bond-loosening) [80]. It is then possible that HCO_3^- / CO_3^{2-} relation could be correlated with the surface pH. On both electrode surfaces, at -0.1 V, the formation of CO_3^{2-} indicates an equilibrium shift and surface pH change toward alkaline conditions. The intensity of the CO_3^{2-} peak is weaker for the low CD electrode, (Figure 6a). However, for the same electrode, increasing the potential cathodically results in the growth of the HCO_3^- peak suggesting HCO_3^- / CO_3^{2-} equilibrium shift back to less alkaline conditions. Accordingly, on the high CD electrode, a slight decrease in surface pH has been also observed. This is simultaneous with the increase in the peak at 750 cm^{-1} (Figure 5b) that is related to the $–CO_3$ group of $Cu_2(CO_3)(OH)_2$ forming on the high CD electrode surface. As a result, in the beginning, less alkaline conditions are required to form $Cu_2(CO_3)(OH)_2$ species, which is consistent with the Pourbaix diagram of $Cu_2(CO_3)(OH)_2$ and $Cu_3(CO_3)_2(OH)_2$ [51,53]. On the same electrode, at -0.9 V the peak intensity of HCO_3^- drops while it stays the same for CO_3^{2-}. This behavior can be an indication of a sudden rise in surface pH associated with emerging of Cu-OH peaks of $Cu_2(CO_3)(OH)_2$ (Figure 5b). This increase in surface pH can be related to the reduction of CO_2 to C2 products and releasing more OH^-, as it is clearly demonstrated in GC-NMR results (Figure 3). Additionally, higher frequency peaks detected at 1178, 1366, 1528, 1587, and 1612 cm^{-1} (I) assigned to carbonate-centered mode vibrations of the $Cu_2(CO_3)(OH)_2$ on top of the high CD electrode, confirming the presence of this specie [53–55,57,79].

In summary, CuO readily forms on the high CD electrode under wet conditions and the surface pH can be presumed to be low due to the absence of CO_3^{2-} in the SERS spectra (Figure S3). However, the application of -0.1 V cathodic potential increases the surface pH (appearance of CO_3^{2-} in the SERS spectra) that provides the condition for the formation of CCH phases. According to the Pourbaix diagram, CCH species form at thermodynamical potentials greater than 0.0 V [53], so the appearance of these species would be expected at positive potentials. Herein, however, we detect this phase at lower potentials. This inconsistency can be justified by a big jump in the potential gradient between the surface and the double layer. The origin of this CCH formation at low potentials can be attributed to the following: (i) slower kinetics of Cu oxide reduction versus CO_2 reduction, (ii) alkaline bulk containing negatively charged ions (OH^-) adjacent to the surface attracting positive ions

building the gradient of the potential, (iii) the presence of the dissolved Cu^{2+} during the reduction [53,54,81]. The open circuit potential in our system over electrodes was measured to be 0.4 V.

Figure 7a shows HCO_3^- / CO_3^{2-} ratios as a function of cathodic potential for low and high CD electrodes. This comparison indicates that, for the high CD electrode, HCO_3^- plays a critical role in the formation of $Cu_2(CO_3)(OH)_2$ phase at all cathodic potentials above -0.2 V. Admittedly, the consumption of HCO_3^- via the formation of $Cu_2(CO_3)(OH)_2$ could reduce its buffering capacity and the shift in the equilibrium can lead to a higher surface pH over the high CD electrode. There is a critical pH value (close to 11) above which a decrease in the CO_2 concentration on the surface can be expected due to CO_2 mass transfer limitations [82–84]. Therefore, reduced buffering capacity of HCO_3^- limit the rate of adsorption of CO_2 on the surface. Figure S4 shows the calculated surface pH (using HCO_3^- / CO_3^{2-} ratio) as a function of potential for both electrodes where the change in buffering capacity of HCO_3^- ions are clearly seen [85,86]. The calculations were derived from Henderson-Hasselbalch equation, assuming that acid-base equilibrium and steady state condition (i.e. concentration of CO_2 remains constant in the continuous purging experiment) are both maintained on the electrocatalyst/electrolyte interface (see SI for the details).

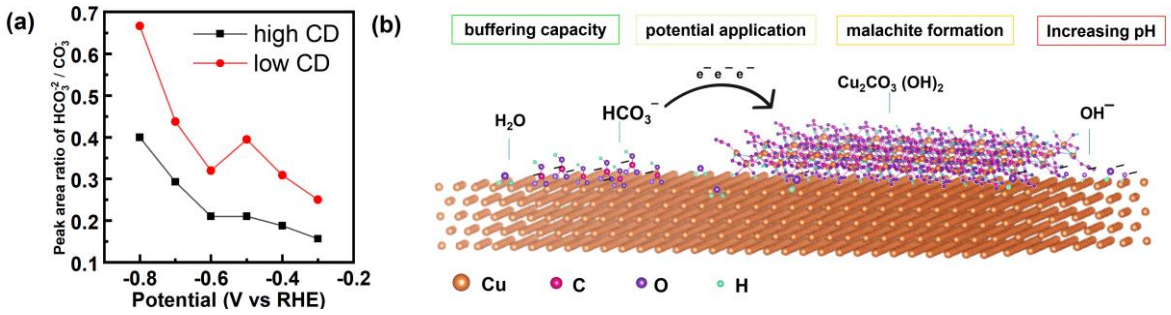


Figure 7. (a) The estimation of the HCO_3^- / CO_3^{2-} peak area ratio as a function of potential. (b) A schematic of the proposed $Cu_2(CO_3)(OH)_2$ formation.

At the same potential applied to both electrodes, the high CD electrode shows a higher reduction current density, which is expected due to its higher electrochemical surface area (Figure S6, Table S3) and porous structure as presented in the SEM image (Figure 1c). This can lead to a higher rate of consumption of protons for HER and CO_2RR and leaving a high concentration of OH^-, further driving higher surface pH over the high CD electrode [58,85,87]. As a result, the surface pH on the interface of this electrode is expected to be higher. On the other hand, if the surface pH has surged to more than a critical value as

explained above, because of the local concentration OH^-, CO_2 depletion can occur (Eq. 1 and 2), giving rise to a drop in the FE of CO_2RR products.

$$CO_2(aq) + OH^- \leftrightarrow HCO_3^- \quad (1)$$

$$HCO_3^- + OH^- \leftrightarrow CO_3^{2-} + H_2O \quad (2)$$

This condition has been noticed on the high CD electrode by rising pH to values higher than 11 at lower potentials. High alkalinity over the high CD electrode can be originated from the buffering reaction not being fulfilled due to the limited availability of HCO_3^- (which has been probably partially consumed for $Cu_2(CO_3)(OH)_2$) and hence local pH was higher than pH in the bulk. The rate of Eq. 2 is much higher than that of Eq. 1 [81], however, the surface transformation on the high CD electrode appears to be playing a more dominant role. Then, it can be concluded that all factors including the structure of the catalyst, availability of the HCO_3^- for buffering, and mass transfer limitation of CO_2 contribute to the higher surface pH of the high CD electrode.

Accordingly, on the surface of the low CD electrode with a relatively lower surface area and current density, higher intensity of HCO_3^- would suggest a relatively lower pH, thus, one can conclude that CO_2 concentration could be higher and the rate of HER will be suppressed. For this electrode, increasing cathodic potentials similarly leads to a decrease in the surface pH (Figure S4) in a limited range. More specifically, high pH observed at all cathodic potentials for both electrodeposited electrodes creates a local environment where the reduction reaction becomes CO_2 mass transfer limited, leading to low FEs of CO_2RR products overall and high FE for HER. These events occurring in the course of the CO_2RR can only be explored by the SERS analysis and are critical for the formation of $Cu_2(CO_3)(OH)_2$ and C2 product selectivity.

Utilization of generated OH^- through reaction with CO_2 near the surface can be considered as a possible motive for moving to less alkalinity by applying higher cathodic potentials (eq. 1). This reaction corroborates the increase in HCO_3^- detected on the surface of both electrodes (but at a different rate) by SERS, which is also a viable donor for HER, over CO_2RR. The detection of HCO_3^- and CO_3^{2-} through SERS and proving their existence suggests that CO_2 has reacted with OH^-. In another experimental study, a similar decrease in pH was noted and described by the reaction of dissolved Cu^{2+} with OH^- and CO_3^{2-} to form $Cu_2(CO_3)(OH)_2$ [88]. In our study, ICP-MS measurements conducted on the electrolyte taken during CO_2RR at -0.8

V for both electrodes showed very low amounts of Cu^{2+} (Table S4). This finding rules out the assumption that the presence of dissolved Cu^{2+} is a requirement for the formation of $Cu_2(CO_3)(OH)_2$ and the consumption of OH^- and CO_3^{2-} to interpret pH behavior going to less alkalinity. If dissolved Cu^{2+} was driving the formation of $Cu_2(CO_3)(OH)_2$, it should have been observed over the low CD electrode, too. However, there was no $Cu_2(CO_3)(OH)_2$ forming on this surface. Moreover, this indicates that low alkalinity at higher cathodic potentials cannot be dependent on OH^- consumption in $Cu_2(CO_3)(OH)_2$ formation. HCO_3^- consumption is a more likely pathway for the formation of $Cu_2(CO_3)(OH)_2$.

To realize if the measured activity improvements are related to the active surface area or due to the advanced intrinsic activity, the partial current densities have been normalized by ECSA (Figure S6 and S7). According to Figure S7a, the ECSA-normalized partial current density of C2 products for the low CD electrode is much higher than that for the high CD electrode. Therefore, the higher C2 efficiency for the low CD electrode is not due to the higher active surface area. Geometrical surface area normalized partial current densities of all products were reported in the SI (Table S6 and Table S7).

Peaks at 890 and 930 cm^{-1} (F) that are assigned to C-C stretching of CH_3COO^- [89] are present on both surfaces, but more pronounced on the high CD electrode (Figure 6). The CH_3COO^- formation mechanism has been explained by the reaction of the weakly adsorbed CO_2^- and CH_3 (at ~2900 cm^{-1},), which are observed species on the high CD electrode, and its evolution was detected by H-NMR at -0.5 V. Intriguingly, CO_2^- has not been observed in low CD spectra, and no CH_3COO^- was detected by H-NMR.

The potential dependent formation of $HCOO^-$ (Figure 3) further show electrode dependency. In Figure 6, adsorbed $HCOO^-$ (J) is identified by the peak at 1295 cm^{-1} (C-H) and the doublet at 1440 and 1460 cm^{-1} (O-bound bidentate intermediate). There are two mechanisms suggested for the formation of $HCOO^-$: proton-coupled electron transfer (PCET) (in the presence of CO_2 and cathodic potential) and hydride (*H) insertion to CO_2 [75,90]. High CD electrode showed PCET intermediates to form $HCOO^-$, which is in accordance with the lack of HCO_3^- involved in the emergence of $Cu_2(CO_3)(OH)_2$. Spectral features of $HCOO^-$ has been clearly depicted in all potentials for the high CD electrode in agreement with its high FE at lower potentials [91], while they appear between -0.5 and -0.9 V with similar noticeable intensity on the low CD electrode on which higher FE of $HCOO^-$ was obtained.

Another noticeable distinction between low CD and high CD electrodes has been observed in the frequency shifts of *CO (1850-2100 cm^{-1}, C–O stretching) clearly detected by the SERS (Figure 8). According to the GC results, the FE of the gaseous CO shows a drop for both electrodes. However, variable frequencies of CO stretching can be spotted over the high CD electrode when the cathodic potential is applied. At the same time, the low FE of C2 products over this electrode can be an indication of a lower chance for CO dimerization. As a result, *CO on a high CD electrode can be attributed to strongly-adsorbed CO. CO poisoning effect has been introduced as one of the reasons for the CO_2 deficiency on the surface of the electrocatalyst [82]. Hydrogen adsorption appears to be more facile than CO_2 in the surface of the high CD electrode on which significant amount of strongly-adsorbed *CO has been observed. Consequently, a higher FE of H_2 is observed over this electrode. On the low CD electrode, CO was detected by GC and its FE dropped at increased cathodic potentials. This FE drop is in accordance with high-frequency CO peaks appearing in SERS spectra and higher FE of C2 products, compared to the high CD electrode. CO dimerization is a crucial step in the formation of C2 products and the adsorption strength of CO plays a defining role in this pathway. The more dominant high frequency of *CO and its lower overall intensity might indicate lower adsorption energy on the surface and can be a sign of dimerization yielding C2 products [41,92]. At -0.7 V, *CO is hardly detected on the low CD electrode surface whereas it is persistent on the high CD electrode even at -0.9 V. It is likely that $Cu_2(CO_3)(OH)_2$ on the surface of the high CD electrode is active for stabilizing *CO, in agreement with the observation of Jiang and co-workers [53]. Concurrent mass transfer limitation of CO_2RR thus leads to the dominance of the HER. Therefore, the protonation of the *CO can have a higher chance to occur, which would pave the way for a decreased FE of the C2 products.

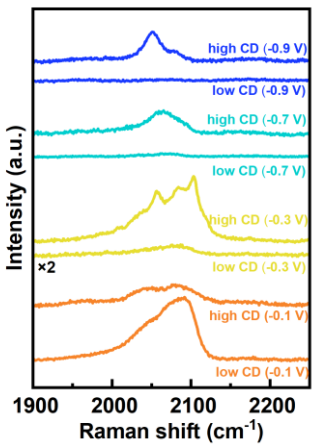


Figure 8. SERS spectra of CO region from two electrodeposited Cu oxide electrodes in CO_2-saturated 0.5 M $KHCO_3$ (pH 7.6) electrolyte solution at various cathodic potentials: To make a clearer comparison, all spectra were background subtracted.

4. Conclusions

In this study, we showed that two electrodeposited Cu oxides (low and high CD) exhibit a considerable gap in FEs of C2 products. In-situ SERS has been employed to monitor the changes in surfaces and surface species in CO_2RR conditions to identify the discrepancy in the FEs of products. SERS investigations under open circuit conditions showed an immediate change in Cu oxidation states of porous high CD electrodes while the low CD electrode remained stable. The product analysis in combination with SERS revealed the correlation between Cu oxidation states, surface intermediates, and the formation of $Cu_2(CO_3)(OH)_2$. Local HCO_3^- concentration and thus pH has an impact on the $Cu_2(CO_3)(OH)_2$ formation which affects adsorbed intermediates and C2 products. $Cu_2(CO_3)(OH)_2$ readily terminates the high CD surface and halts the further CO_2RR. Another consequence of the $Cu_2(CO_3)(OH)_2$ formation is the elimination of HCO_3^- ions and the change in the buffering capacity near the surface of the high CD electrode. HCO_3^- consumption causes higher alkalinity persisting over this electrode, leading to a low CO_2 concentration near the surface and intensifies HER at the expense of C2 products. Strongly adsorbed CO molecules over the high CD electrode terminated by $Cu_2(CO_3)(OH)_2$ could be responsible for the elimination of the C2 pathway. Overall, this study provides critical insights into the electrocatalytic CO_2RR over Cu oxides. In-situ SERS investigations could be beneficial for identifying surface species and deciphering different mechanisms in CO_2RR. This information can be utilized for prospective studies to optimize a more efficient electrocatalyst and to reach the desired selectivity.

Acknowledgments

The authors would like to thank The Scientific and Technical Research Council of Turkey (TUBITAK) for support (Grant number: 118Z740). The authors thank KUYTAM for the characterization measurements.

Conflict of Interest

The authors declare no conflict of interest.

References

[1] I.E.L. Stephens, K. Chan, A. Bagger, S.W. Boettcher, J. Bonin, E. Boutin, A. Buckley, R. Buonsanti, E. Cave, X. Chang, S.W. Chee, A.H.M. da Silva, P. De Luna, O. Einsle, B. Endrődi, M.E. Escribano, J.V. Ferreira de Araujo, M.C. Figueiredo, C. Hahn, K.U. Hansen, S. Haussener, S. Hunegnaw, Z. Huo, Y.J.

Hwang, C. Janáky, B.S. Jayathilake, F. Jiao, Z.P. Jovanov, P. Karimi, M.T.M. Koper, K. Kuhl, W.H. Lee, Z. Liang, X. Liu, S. Ma, M. Ma, H.-S. Oh, M. Robert, B.R. Cuenya, J. Rossmeisl, C. Roy, M.P. Ryan, E.H. Sargent, P. Sebastián-Pascual, B. Seger, L. Steier, P. Strasser, A.S. Varela, R.E. Vos, X. Wang, B. Xu, H. Yadegari, Y. Zhou, 2022 Roadmap on Low Temperature Electrochemical CO2 Reduction, J. Phys. Energy. (2022). https://doi.org/10.1088/2515-7655/ac7823.

[2] M. Sassenburg, R. de Rooij, N.T. Nesbitt, R. Kas, S. Chandrashekar, N.J. Firet, K. Yang, K. Liu, M.A. Blommaert, M. Kolen, D. Ripepi, W.A. Smith, T. Burdyny, Characterizing CO2 Reduction Catalysts on Gas Diffusion Electrodes: Comparing Activity, Selectivity, and Stability of Transition Metal Catalysts, ACS Appl. Energy Mater. 5 (2022) 5983–5994. https://doi.org/10.1021/acsaem.2c00160.

[3] S. Lu, Y. Wang, H. Xiang, H. Lei, B.B. Xu, L. Xing, E.H. Yu, T.X. Liu, Mass transfer effect to electrochemical reduction of CO2: Electrode, electrocatalyst and electrolyte, J. Energy Storage. 52 (2022) 104764. https://doi.org/10.1016/j.est.2022.104764.

[4] E. Ruiz-López, J. Gandara-Loe, F. Baena-Moreno, T.R. Reina, J.A. Odriozola, Electrocatalytic CO2 conversion to C2 products: Catalysts design, market perspectives and techno-economic aspects, Renew. Sustain. Energy Rev. 161 (2022) 112329. https://doi.org/10.1016/j.rser.2022.112329.

[5] X. Wang, Z. Wang, F.P. García de Arquer, C.-T. Dinh, A. Ozden, Y.C. Li, D.-H. Nam, J. Li, Y.-S. Liu, J. Wicks, Z. Chen, M. Chi, B. Chen, Y. Wang, J. Tam, J.Y. Howe, A. Proppe, P. Todorović, F. Li, T.-T. Zhuang, C.M. Gabardo, A.R. Kirmani, C. McCallum, S.-F. Hung, Y. Lum, M. Luo, Y. Min, A. Xu, C.P. O'Brien, B. Stephen, B. Sun, A.H. Ip, L.J. Richter, S.O. Kelley, D. Sinton, E.H. Sargent, Efficient electrically powered CO2-to-ethanol via suppression of deoxygenation, Nat. Energy. 5 (2020) 478–486. https://doi.org/10.1038/s41560-020-0607-8.

[6] C.W. Li, M.W. Kanan, CO2 Reduction at Low Overpotential on Cu Electrodes Resulting from the Reduction of Thick Cu2O Films, J. Am. Chem. Soc. 134 (2012) 7231–7234. https://doi.org/10.1021/ja3010978.

[7] P. De Luna, R. Quintero-Bermudez, C.-T. Dinh, M.B. Ross, O.S. Bushuyev, P. Todorović, T. Regier, S.O. Kelley, P. Yang, E.H. Sargent, Catalyst electro-redeposition controls morphology and oxidation state for selective carbon dioxide reduction, Nat. Catal. 1 (2018) 103–110. https://doi.org/10.1038/s41929-017-0018-9.

[8] T.-C. Chou, C.-C. Chang, H.-L. Yu, W.-Y. Yu, C.-L. Dong, J.-J. Velasco-Vélez, C.-H. Chuang, L.-C. Chen, J.-F. Lee, J.-M. Chen, H.-L. Wu, Controlling the Oxidation State of the Cu Electrode and Reaction Intermediates for Electrochemical CO_2 Reduction to Ethylene, J. Am. Chem. Soc. 142 (2020) 2857–2867. https://doi.org/10.1021/jacs.9b11126.

[9] P.-P. Yang, X.-L. Zhang, F.-Y. Gao, Y.-R. Zheng, Z.-Z. Niu, X. Yu, R. Liu, Z.-Z. Wu, S. Qin, L.-P. Chi, Y. Duan, T. Ma, X.-S. Zheng, J.-F. Zhu, H.-J. Wang, M.-R. Gao, S.-H. Yu, Protecting Copper Oxidation State via Intermediate Confinement for Selective CO_2 Electroreduction to C_{2+} Fuels, J. Am. Chem. Soc. 142 (2020) 6400–6408. https://doi.org/10.1021/jacs.0c01699.

[10] J.-J. Velasco-Velez, R.V. Mom, L.-E. Sandoval-Diaz, L.J. Falling, C.-H. Chuang, D. Gao, T.E. Jones, Q. Zhu, R. Arrigo, B. Roldan Cuenya, A. Knop-Gericke, T. Lunkenbein, R. Schlögl, Revealing the Active Phase of Copper during the Electroreduction of CO2 in Aqueous Electrolyte by Correlating In Situ X-ray Spectroscopy and In Situ Electron Microscopy, ACS Energy Lett. 5 (2020) 2106–2111. https://doi.org/10.1021/acsenergylett.0c00802.

[11] T. Möller, F. Scholten, T.N. Thanh, I. Sinev, J. Timoshenko, X. Wang, Z. Jovanov, M. Gliech, B. Roldan Cuenya, A.S. Varela, P. Strasser, Electrocatalytic CO2 Reduction on CuOx Nanocubes: Tracking the Evolution of Chemical State, Geometric Structure, and Catalytic Selectivity using Operando Spectroscopy, Angew. Chem. 132 (2020) 18130–18139. https://doi.org/10.1002/ange.202007136.

[12] R. Zhang, F. Chen, H. Jin, Y. Zhang, X. Hao, Y. Liu, T. Feng, X. Zhang, Z. Lu, W. Wang, F. Lu, H. Dong, H. Liu, H. Liu, Y. Cheng, Highly stability Cu+ species in hollow Cu2O nanoreactors by modulating cavity size for CO2 electroreduction to C2+ products, Chem. Eng. J. 461 (2023) 142052. https://doi.org/10.1016/j.cej.2023.142052.

[13] X. Chang, M. He, Q. Lu, B. Xu, Origin and effect of surface oxygen-containing species on electrochemical CO or CO2 reduction reactions, Sci. China Chem. 66 (2023) 96–106. https://doi.org/10.1007/s11426-022-1459-3.

[14] A.D. Handoko, C.W. Ong, Y. Huang, Z.G. Lee, L. Lin, G.B. Panetti, B.S. Yeo, Mechanistic Insights into the Selective Electroreduction of Carbon Dioxide to Ethylene on Cu2O-Derived Copper Catalysts, J. Phys. Chem. C. 120 (2016) 20058–20067. https://doi.org/10.1021/acs.jpcc.6b07128.

[15] M. Wang, Q. Zhang, Q. Xie, L. Wan, Y. Zhao, X. Zhang, J. Luo, Selective electrochemical reduction of carbon dioxide to ethylene on a copper hydroxide nitrate nanostructure electrode, Nanoscale. 12 (2020) 17013–17019. https://doi.org/10.1039/D0NR02591G.

[16] S. Chu, X. Yan, C. Choi, S. Hong, A.W. Robertson, J. Masa, B. Han, Y. Jung, Z. Sun, Stabilization of Cu $^{+}$ by tuning a CuO–CeO $_{2}$ interface for selective electrochemical CO $_{2}$ reduction to ethylene, Green Chem. 22 (2020) 6540–6546. https://doi.org/10.1039/D0GC02279A.
[17] X. Su, Y. Sun, L. Jin, L. Zhang, Y. Yang, P. Kerns, B. Liu, S. Li, J. He, Hierarchically porous Cu/Zn bimetallic catalysts for highly selective CO2 electroreduction to liquid C2 products, Appl. Catal. B Environ. 269 (2020) 118800. https://doi.org/10.1016/j.apcatb.2020.118800.
[18] A. Eilert, F. Cavalca, F.S. Roberts, J. Osterwalder, C. Liu, M. Favaro, E.J. Crumlin, H. Ogasawara, D. Friebel, L.G.M. Pettersson, A. Nilsson, Subsurface Oxygen in Oxide-Derived Copper Electrocatalysts for Carbon Dioxide Reduction, J. Phys. Chem. Lett. 8 (2017) 285–290. https://doi.org/10.1021/acs.jpclett.6b02273.
[19] M. Favaro, H. Xiao, T. Cheng, W.A. Goddard, J. Yano, E.J. Crumlin, Subsurface oxide plays a critical role in CO2 activation by Cu(111) surfaces to form chemisorbed CO2, the first step in reduction of CO2, Proc. Natl. Acad. Sci. 114 (2017) 6706–6711. https://doi.org/10.1073/pnas.1701405114.
[20] H. Mistry, A.S. Varela, C.S. Bonifacio, I. Zegkinoglou, I. Sinev, Y.-W. Choi, K. Kisslinger, E.A. Stach, J.C. Yang, P. Strasser, B.R. Cuenya, Highly selective plasma-activated copper catalysts for carbon dioxide reduction to ethylene, Nat. Commun. 7 (2016) 12123. https://doi.org/10.1038/ncomms12123.
[21] M. Le, M. Ren, Z. Zhang, P.T. Sprunger, R.L. Kurtz, J.C. Flake, Electrochemical Reduction of CO2 to CH3OH at Copper Oxide Surfaces, J. Electrochem. Soc. 158 (2011) E45. https://doi.org/10.1149/1.3561636.
[22] D. Kim, S. Lee, J.D. Ocon, B. Jeong, J.K. Lee, J. Lee, Insights into an autonomously formed oxygen-evacuated Cu2O electrode for the selective production of C2H4 from CO2, Phys. Chem. Chem. Phys. 17 (2014) 824–830. https://doi.org/10.1039/C4CP03172E.
[23] X. Nie, G.L. Griffin, M.J. Janik, A. Asthagiri, Surface phases of Cu2O(111) under CO2 electrochemical reduction conditions, Catal. Commun. 52 (2014) 88–91. https://doi.org/10.1016/j.catcom.2014.02.022.
[24] D. Gao, I. Zegkinoglou, N.J. Divins, F. Scholten, I. Sinev, P. Grosse, B. Roldan Cuenya, Plasma-Activated Copper Nanocube Catalysts for Efficient Carbon Dioxide Electroreduction to Hydrocarbons and Alcohols, ACS Nano. 11 (2017) 4825–4831. https://doi.org/10.1021/acsnano.7b01257.
[25] X. Chang, J. Li, H. Xiong, H. Zhang, Y. Xu, H. Xiao, Q. Lu, B. Xu, C−C Coupling Is Unlikely to Be the Rate-Determining Step in the Formation of C2+ Products in the Copper-Catalyzed Electrochemical Reduction of CO, Angew. Chem. Int. Ed. 61 (2022) e202111167. https://doi.org/10.1002/anie.202111167.
[26] F. Scholten, K.-L.C. Nguyen, J.P. Bruce, M. Heyde, B. Roldan Cuenya, Identifying Structure–Selectivity Correlations in the Electrochemical Reduction of CO2: A Comparison of Well-Ordered Atomically Clean and Chemically Etched Copper Single-Crystal Surfaces, Angew. Chem. Int. Ed. 60 (2021) 19169–19175. https://doi.org/10.1002/anie.202103102.
[27] F. Scholten, I. Sinev, M. Bernal, B. Roldan Cuenya, Plasma-Modified Dendritic Cu Catalyst for CO2 Electroreduction, ACS Catal. 9 (2019) 5496–5502. https://doi.org/10.1021/acscatal.9b00483.
[28] A.A. Permyakova, J. Herranz, M. El Kazzi, J.S. Diercks, M. Povia, L.R. Mangani, M. Horisberger, A. Pătru, T.J. Schmidt, On the Oxidation State of Cu2O upon Electrochemical CO2 Reduction: An XPS Study, ChemPhysChem. 20 (2019) 3120–3127. https://doi.org/10.1002/cphc.201900468.
[29] M. Moradzaman, G. Mul, In Situ Raman Study of Potential-Dependent Surface Adsorbed Carbonate, CO, OH, and C Species on Cu Electrodes During Electrochemical Reduction of CO $_{2}$, ChemElectroChem. 8 (2021) 1478–1485. https://doi.org/10.1002/celc.202001598.
[30] A. Dutta, M. Rahaman, B. Hecker, J. Drnec, K. Kiran, I. Zelocualtecatl Montiel, D. Jochen Weber, A. Zanetti, A. Cedeño López, I. Martens, P. Broekmann, M. Oezaslan, CO2 electrolysis – Complementary operando XRD, XAS and Raman spectroscopy study on the stability of CuxO foam catalysts, J. Catal. 389 (2020) 592–603. https://doi.org/10.1016/j.jcat.2020.06.024.
[31] X. Chang, Y. Zhao, B. Xu, pH Dependence of Cu Surface Speciation in the Electrochemical CO Reduction Reaction, ACS Catal. 10 (2020) 13737–13747. https://doi.org/10.1021/acscatal.0c03108.
[32] Y. Zhao, X. Chang, A.S. Malkani, X. Yang, L. Thompson, F. Jiao, B. Xu, Speciation of Cu Surfaces During the Electrochemical CO Reduction Reaction, J. Am. Chem. Soc. (2020) jacs.0c02354. https://doi.org/10.1021/jacs.0c02354.
[33] H. Jiang, Q. He, Y. Zhang, L. Song, Structural Self-Reconstruction of Catalysts in Electrocatalysis, Acc. Chem. Res. 51 (2018) 2968–2977. https://doi.org/10.1021/acs.accounts.8b00449.
[34] H. An, L. Wu, L.D.B. Mandemaker, S. Yang, J. Ruiter, J.H.J. Wijten, J.C.L. Janssens, T. Hartman, W. Stam, B.M. Weckhuysen, Sub-Second Time-Resolved Surface-Enhanced Raman Spectroscopy Reveals Dynamic CO Intermediates during Electrochemical CO $_{2}$ Reduction on Copper, Angew. Chem. Int. Ed. 60 (2021) 16576–16584. https://doi.org/10.1002/anie.202104114.
[35] M. He, C. Li, H. Zhang, X. Chang, J.G. Chen, W.A. Goddard, M. Cheng, B. Xu, Q. Lu, Oxygen induced promotion of electrochemical reduction of CO2 via co-electrolysis, Nat. Commun. 11 (2020) 3844. https://doi.org/10.1038/s41467-020-17690-8.

[36] A.J. Garza, A.T. Bell, M. Head-Gordon, Is Subsurface Oxygen Necessary for the Electrochemical Reduction of CO2 on Copper?, J. Phys. Chem. Lett. 9 (2018) 601–606. https://doi.org/10.1021/acs.jpclett.7b03180.
[37] D. Devasia, A.J. Wilson, J. Heo, V. Mohan, P.K. Jain, A rich catalog of C–C bonded species formed in CO2 reduction on a plasmonic photocatalyst, Nat. Commun. 12 (2021) 2612. https://doi.org/10.1038/s41467-021-22868-9.
[38] L. Jin, A. Seifitokaldani, In Situ Spectroscopic Methods for Electrocatalytic CO2 Reduction, Catalysts. 10 (2020) 481. https://doi.org/10.3390/catal10050481.
[39] Y.C. Li, Z. Wang, T. Yuan, D.-H. Nam, M. Luo, J. Wicks, B. Chen, J. Li, F. Li, F.P.G. de Arquer, Y. Wang, C.-T. Dinh, O. Voznyy, D. Sinton, E.H. Sargent, Binding Site Diversity Promotes CO2 Electroreduction to Ethanol, J. Am. Chem. Soc. 141 (2019) 8584–8591. https://doi.org/10.1021/jacs.9b02945.
[40] J.C. Hamilton, J.C. Farmer, R.J. Anderson, In Situ Raman Spectroscopy of Anodic Films Formed on Copper and Silver in Sodium Hydroxide Solution, J. Electrochem. Soc. 133 (1986) 739. https://doi.org/10.1149/1.2108666.
[41] H. An, L. Wu, L.D.B. Mandemaker, S. Yang, J. Ruiter, J.H.J. Wijten, J.C.L. Janssens, T. Hartman, W. Stam, B.M. Weckhuysen, Sub-Second Time-Resolved Surface-Enhanced Raman Spectroscopy Reveals Dynamic CO Intermediates during Electrochemical CO_2 Reduction on Copper, Angew. Chem. Int. Ed. 60 (2021) 16576–16584. https://doi.org/10.1002/anie.202104114.
[42] H.Y.H. Chan, C.G. Takoudis, M.J. Weaver, Oxide Film Formation and Oxygen Adsorption on Copper in Aqueous Media As Probed by Surface-Enhanced Raman Spectroscopy, J. Phys. Chem. B. 103 (1999) 357–365. https://doi.org/10.1021/jp983787c.
[43] S. Jiang, K. Klingan, C. Pasquini, H. Dau, New aspects of operando Raman spectroscopy applied to electrochemical CO_2 reduction on Cu foams, J. Chem. Phys. 150 (2019) 041718. https://doi.org/10.1063/1.5054109.
[44] B.D. Smith, D.E. Irish, P. Kedzierzawski, J. Augustynski, A Surface Enhanced Raman Scattering Study of the Intermediate and Poisoning Species Formed during the Electrochemical Reduction of CO2 on Copper, J Electrochem Soc. 144 (1997) 9.
[45] D.A. Svintsitskiy, A.I. Stadnichenko, D.V. Demidov, S.V. Koscheev, A.I. Boronin, Investigation of oxygen states and reactivities on a nanostructured cupric oxide surface, Appl. Surf. Sci. 257 (2011) 8542–8549. https://doi.org/10.1016/j.apsusc.2011.05.012.
[46] C. Zhu, A. Osherov, M.J. Panzer, Surface chemistry of electrodeposited Cu2O films studied by XPS, Electrochimica Acta. 111 (2013) 771–778. https://doi.org/10.1016/j.electacta.2013.08.038.
[47] H. Guzmán, F. Zammillo, D. Roldán, C. Galletti, N. Russo, S. Hernández, Investigation of Gas Diffusion Electrode Systems for the Electrochemical CO2 Conversion, Catalysts. 11 (2021) 482. https://doi.org/10.3390/catal11040482.
[48] M. Samouhos, R. Hutcheon, I. Paspaliaris, Microwave reduction of copper(II) oxide and malachite concentrate, Miner. Eng. 24 (2011) 903–913. https://doi.org/10.1016/j.mineng.2011.03.026.
[49] Q. Lei, L. Huang, J. Yin, B. Davaasuren, Y. Yuan, X. Dong, Z.-P. Wu, X. Wang, K.X. Yao, X. Lu, Y. Han, Structural evolution and strain generation of derived-Cu catalysts during CO2 electroreduction, Nat. Commun. 13 (2022) 4857. https://doi.org/10.1038/s41467-022-32601-9.
[50] W. Gao, G. Qu, Xu M., S. Chang, W. Na, Effect of pH on Co-precipitated Cu-ZnO-ZrO2 Catalysts Used in CO2 Hydrogenation: the Role of Zn-malachite in the Precursors▲, Fuel Cells. 21 (2021) 31–38. https://doi.org/10.1002/fuce.202000032.
[51] J.-J. Velasco-Vélez, T. Jones, D. Gao, E. Carbonio, R. Arrigo, C.-J. Hsu, Y.-C. Huang, C.-L. Dong, J.-M. Chen, J.-F. Lee, P. Strasser, B. Roldan Cuenya, R. Schlögl, A. Knop-Gericke, C.-H. Chuang, The Role of the Copper Oxidation State in the Electrocatalytic Reduction of CO2 into Valuable Hydrocarbons, ACS Sustain. Chem. Eng. 7 (2019) 1485–1492. https://doi.org/10.1021/acssuschemeng.8b05106.
[52] A. Eilert, F.S. Roberts, D. Friebel, A. Nilsson, Formation of Copper Catalysts for CO2 Reduction with High Ethylene/Methane Product Ratio Investigated with In Situ X-ray Absorption Spectroscopy, J. Phys. Chem. Lett. 7 (2016) 1466–1470. https://doi.org/10.1021/acs.jpclett.6b00367.
[53] S. Jiang, L. D'Amario, H. Dau, Copper Carbonate Hydroxide as Precursor of Interfacial CO in CO2 Electroreduction, ChemSusChem. 15 (2022) e202102506. https://doi.org/10.1002/cssc.202102506.
[54] D.A. Henckel, M.J. Counihan, H.E. Holmes, X. Chen, U.O. Nwabara, S. Verma, J. Rodríguez-López, P.J.A. Kenis, A.A. Gewirth, Potential Dependence of the Local pH in a CO2 Reduction Electrolyzer, ACS Catal. 11 (2021) 255–263. https://doi.org/10.1021/acscatal.0c04297.
[55] M. Spodaryk, K. Zhao, J. Zhang, E. Oveisi, A. Züttel, The role of malachite nanorods for the electrochemical reduction of CO2 to C2 hydrocarbons, Electrochimica Acta. 297 (2019) 55–60. https://doi.org/10.1016/j.electacta.2018.11.124.

[56] B. Liu, X. Yao, Z. Zhang, C. Li, J. Zhang, P. Wang, J. Zhao, Y. Guo, J. Sun, C. Zhao, Synthesis of Cu2O Nanostructures with Tunable Crystal Facets for Electrochemical CO2 Reduction to Alcohols, ACS Appl. Mater. Interfaces. 13 (2021) 39165–39177. https://doi.org/10.1021/acsami.1c03850.
[57] Q. Zhu, X. Sun, D. Yang, J. Ma, X. Kang, L. Zheng, J. Zhang, Z. Wu, B. Han, Carbon dioxide electroreduction to C2 products over copper-cuprous oxide derived from electrosynthesized copper complex, Nat. Commun. 10 (2019) 3851. https://doi.org/10.1038/s41467-019-11599-7.
[58] Y. Lum, B. Yue, P. Lobaccaro, A.T. Bell, J.W. Ager, Optimizing C–C Coupling on Oxide-Derived Copper Catalysts for Electrochemical CO_2 Reduction, J. Phys. Chem. C. 121 (2017) 14191–14203. https://doi.org/10.1021/acs.jpcc.7b03673.
[59] Y. Lum, J.W. Ager, Stability of Residual Oxides in Oxide-Derived Copper Catalysts for Electrochemical CO2 Reduction Investigated with 18O Labeling, Angew. Chem. Int. Ed. 57 (2018) 551–554. https://doi.org/10.1002/anie.201710590.
[60] A.S. ELmezayyen, S. Guan, F.M. Reicha, I.M. El-Sherbiny, jianming Zheng, C. Xu, Effect of conductive substrate (working electrode) on the morphology of electrodeposited Cu$\less$sub$\greater$2$\less$/sub$\greater$O, J. Phys. Appl. Phys. 48 (2015) 175502. https://doi.org/10.1088/0022-3727/48/17/175502.
[61] S. Sun, X. Zhang, Q. Yang, S. Liang, X. Zhang, Z. Yang, Cuprous oxide (Cu2O) crystals with tailored architectures: A comprehensive review on synthesis, fundamental properties, functional modifications and applications, Prog. Mater. Sci. 96 (2018) 111–173. https://doi.org/10.1016/j.pmatsci.2018.03.006.
[62] F. Hu, K.C. Chan, T.M. Yue, Morphology and growth of electrodeposited cuprous oxide under different values of direct current density, Thin Solid Films. 518 (2009) 120–125. https://doi.org/10.1016/j.tsf.2009.07.010.
[63] P. Grosse, A. Yoon, C. Rettenmaier, A. Herzog, S.W. Chee, B. Roldan Cuenya, Dynamic transformation of cubic copper catalysts during CO2 electroreduction and its impact on catalytic selectivity, Nat. Commun. 12 (2021) 6736. https://doi.org/10.1038/s41467-021-26743-5.
[64] J. Huang, N. Hörmann, E. Oveisi, A. Loiudice, G.L. De Gregorio, O. Andreussi, N. Marzari, R. Buonsanti, Potential-induced nanoclustering of metallic catalysts during electrochemical CO2 reduction, Nat. Commun. 9 (2018) 3117. https://doi.org/10.1038/s41467-018-05544-3.
[65] J. Resasco, Y. Lum, E. Clark, J.Z. Zeledon, A.T. Bell, Effects of Anion Identity and Concentration on Electrochemical Reduction of CO2, ChemElectroChem. 5 (2018) 1064–1072. https://doi.org/10.1002/celc.201701316.
[66] A.M. Asiri, J. Gao, S.B. Khan, K.A. Alamry, H.M. Marwani, M.S.J. Khan, W.A. Adeosun, S.M. Zakeeruddin, D. Ren, M. Grätzel, Revisiting the Impact of Morphology and Oxidation State of Cu on CO2 Reduction Using Electrochemical Flow Cell, J. Phys. Chem. Lett. 13 (2022) 345–351. https://doi.org/10.1021/acs.jpclett.1c03957.
[67] T.T.H. Hoang, S. Ma, J.I. Gold, P.J.A. Kenis, A.A. Gewirth, Nanoporous Copper Films by Additive-Controlled Electrodeposition: CO_2 Reduction Catalysis, ACS Catal. 7 (2017) 3313–3321. https://doi.org/10.1021/acscatal.6b03613.
[68] J.H. Montoya, C. Shi, K. Chan, J.K. Nørskov, Theoretical Insights into a CO Dimerization Mechanism in CO2 Electroreduction, J. Phys. Chem. Lett. 6 (2015) 2032–2037. https://doi.org/10.1021/acs.jpclett.5b00722.
[69] K.J.P. Schouten, Z. Qin, E. Pérez Gallent, M.T.M. Koper, Two Pathways for the Formation of Ethylene in CO Reduction on Single-Crystal Copper Electrodes, J. Am. Chem. Soc. 134 (2012) 9864–9867. https://doi.org/10.1021/ja302668n.
[70] R.M. Arán-Ais, F. Scholten, S. Kunze, R. Rizo, B. Roldan Cuenya, The role of in situ generated morphological motifs and Cu(i) species in C2+ product selectivity during CO2 pulsed electroreduction, Nat. Energy. 5 (2020) 317–325. https://doi.org/10.1038/s41560-020-0594-9.
[71] K. Jiang, R.B. Sandberg, A.J. Akey, X. Liu, D.C. Bell, J.K. Nørskov, K. Chan, H. Wang, Metal ion cycling of Cu foil for selective C–C coupling in electrochemical CO2 reduction, Nat. Catal. 1 (2018) 111–119. https://doi.org/10.1038/s41929-017-0009-x.
[72] J. Wang, T. Cheng, A.Q. Fenwick, T.N. Baroud, A. Rosas-Hernández, J.H. Ko, Q. Gan, W.A. Goddard III, R.H. Grubbs, Selective CO_2 Electrochemical Reduction Enabled by a Tricomponent Copolymer Modifier on a Copper Surface, J. Am. Chem. Soc. 143 (2021) 2857–2865. https://doi.org/10.1021/jacs.0c12478.
[73] L. Debbichi, M.C. Marco de Lucas, J.F. Pierson, P. Krüger, Vibrational Properties of CuO and Cu4O3 from First-Principles Calculations, and Raman and Infrared Spectroscopy, J. Phys. Chem. C. 116 (2012) 10232–10237. https://doi.org/10.1021/jp303096m.
[74] V.S. Bryantsev, M.S. Diallo, A.C.T. van Duin, W.A. Goddard III, Hydration of Copper(II): New Insights from Density Functional Theory and the COSMO Solvation Model, J. Phys. Chem. A. 112 (2008) 9104–9112. https://doi.org/10.1021/jp804373p.

[75] I.V. Chernyshova, P. Somasundaran, S. Ponnurangam, On the origin of the elusive first intermediate of CO_2 electroreduction, Proc. Natl. Acad. Sci. 115 (2018). https://doi.org/10.1073/pnas.1802256115.
[76] Y. Deng, B.S. Yeo, Characterization of Electrocatalytic Water Splitting and CO_2 Reduction Reactions Using In Situ/Operando Raman Spectroscopy, ACS Catal. 7 (2017) 7873–7889. https://doi.org/10.1021/acscatal.7b02561.
[77] C. Zhan, F. Dattila, C. Rettenmaier, A. Bergmann, S. Kühl, R. García-Muelas, N. López, B.R. Cuenya, Revealing the CO Coverage-Driven C–C Coupling Mechanism for Electrochemical CO_2 Reduction on Cu_2O Nanocubes *via Operando* Raman Spectroscopy, ACS Catal. 11 (2021) 7694–7701. https://doi.org/10.1021/acscatal.1c01478.
[78] D. Ren, J. Gao, S.M. Zakeeruddin, M. Grätzel, New Insights into the Interface of Electrochemical Flow Cells for Carbon Dioxide Reduction to Ethylene, J. Phys. Chem. Lett. 12 (2021) 7583–7589. https://doi.org/10.1021/acs.jpclett.1c02043.
[79] J.A. Goldsmith, S.D. Ross, The infra-red spectra of azurite and malachite, Spectrochim. Acta Part Mol. Spectrosc. 24 (1968) 2131–2137. https://doi.org/10.1016/0584-8539(68)80273-9.
[80] G. Bublitz, S. Boxer, Stark Spectroscopy: Applications in Chemistry, Biology, and Materials Science, Annu. Rev. Phys. Chem. 48 (1997) 213–42. https://doi.org/10.1146/annurev.physchem.48.1.213.
[81] M. Dunwell, X. Yang, B.P. Setzler, J. Anibal, Y. Yan, B. Xu, Examination of Near-Electrode Concentration Gradients and Kinetic Impacts on the Electrochemical Reduction of CO2 using Surface-Enhanced Infrared Spectroscopy, ACS Catal. 8 (2018) 3999–4008. https://doi.org/10.1021/acscatal.8b01032.
[82] D. Raciti, M. Mao, J.H. Park, C. Wang, Local pH Effect in the CO_2 Reduction Reaction on High-Surface-Area Copper Electrocatalysts, J. Electrochem. Soc. 165 (2018) F799–F804. https://doi.org/10.1149/2.0521810jes.
[83] C.F.C. Lim, D.A. Harrington, A.T. Marshall, Effects of mass transfer on the electrocatalytic CO2 reduction on Cu, Electrochimica Acta. 238 (2017) 56–63. https://doi.org/10.1016/j.electacta.2017.04.017.
[84] D. Raciti, M. Mao, J.H. Park, C. Wang, Mass transfer effects in CO2 reduction on Cu nanowire electrocatalysts, Catal. Sci. Technol. 8 (2018) 2364–2369. https://doi.org/10.1039/C8CY00372F.
[85] N. Gupta, M. Gattrell, B. MacDougall, Calculation for the cathode surface concentrations in the electrochemical reduction of CO2 in KHCO3 solutions, J. Appl. Electrochem. 36 (2006) 161–172. https://doi.org/10.1007/s10800-005-9058-y.
[86] A.S. Varela, M. Kroschel, T. Reier, P. Strasser, Controlling the selectivity of CO2 electroreduction on copper: The effect of the electrolyte concentration and the importance of the local pH, Catal. Today. 260 (2016) 8–13. https://doi.org/10.1016/j.cattod.2015.06.009.
[87] Y. Hori, A. Murata, R. Takahashi, Formation of hydrocarbons in the electrochemical reduction of carbon dioxide at a copper electrode in aqueous solution, J. Chem. Soc. Faraday Trans. 1 Phys. Chem. Condens. Phases. 85 (1989) 2309. https://doi.org/10.1039/f19898502309.
[88] D.A. Henckel, M.J. Counihan, H.E. Holmes, X. Chen, U.O. Nwabara, S. Verma, J. Rodríguez-López, P.J.A. Kenis, A.A. Gewirth, Potential Dependence of the Local pH in a CO_2 Reduction Electrolyzer, ACS Catal. 11 (2021) 255–263. https://doi.org/10.1021/acscatal.0c04297.
[89] T. Nakabayashi, K. Kosugi, N. Nishi, Liquid Structure of Acetic Acid Studied by Raman Spectroscopy and Ab Initio Molecular Orbital Calculations, J. Phys. Chem. A. 103 (1999) 8595–8603. https://doi.org/10.1021/jp991501d.
[90] D. Bohra, I. Ledezma-Yanez, G. Li, W. de Jong, E.A. Pidko, W.A. Smith, Lateral Adsorbate Interactions Inhibit $HCOO^-$ while Promoting CO Selectivity for CO_2 Electrocatalysis on Silver, Angew. Chem. 131 (2019) 1359–1363. https://doi.org/10.1002/ange.201811667.
[91] R. Kortlever, J. Shen, K.J.P. Schouten, F. Calle-Vallejo, M.T.M. Koper, Catalysts and Reaction Pathways for the Electrochemical Reduction of Carbon Dioxide, J. Phys. Chem. Lett. 6 (2015) 4073–4082. https://doi.org/10.1021/acs.jpclett.5b01559.
[92] K.G. Schmitt, A.A. Gewirth, In Situ Surface-Enhanced Raman Spectroscopy of the Electrochemical Reduction of Carbon Dioxide on Silver with 3,5-Diamino-1,2,4-Triazole, J. Phys. Chem. C. 118 (2014) 17567–17576. https://doi.org/10.1021/jp503598y.